Supplementary Material for

Achieving 12.7% energy conversion efficiency in segmented GeTe/BST-SKD thermoelectric modules via broad-temperature and structure optimizations

Supplementary Figures

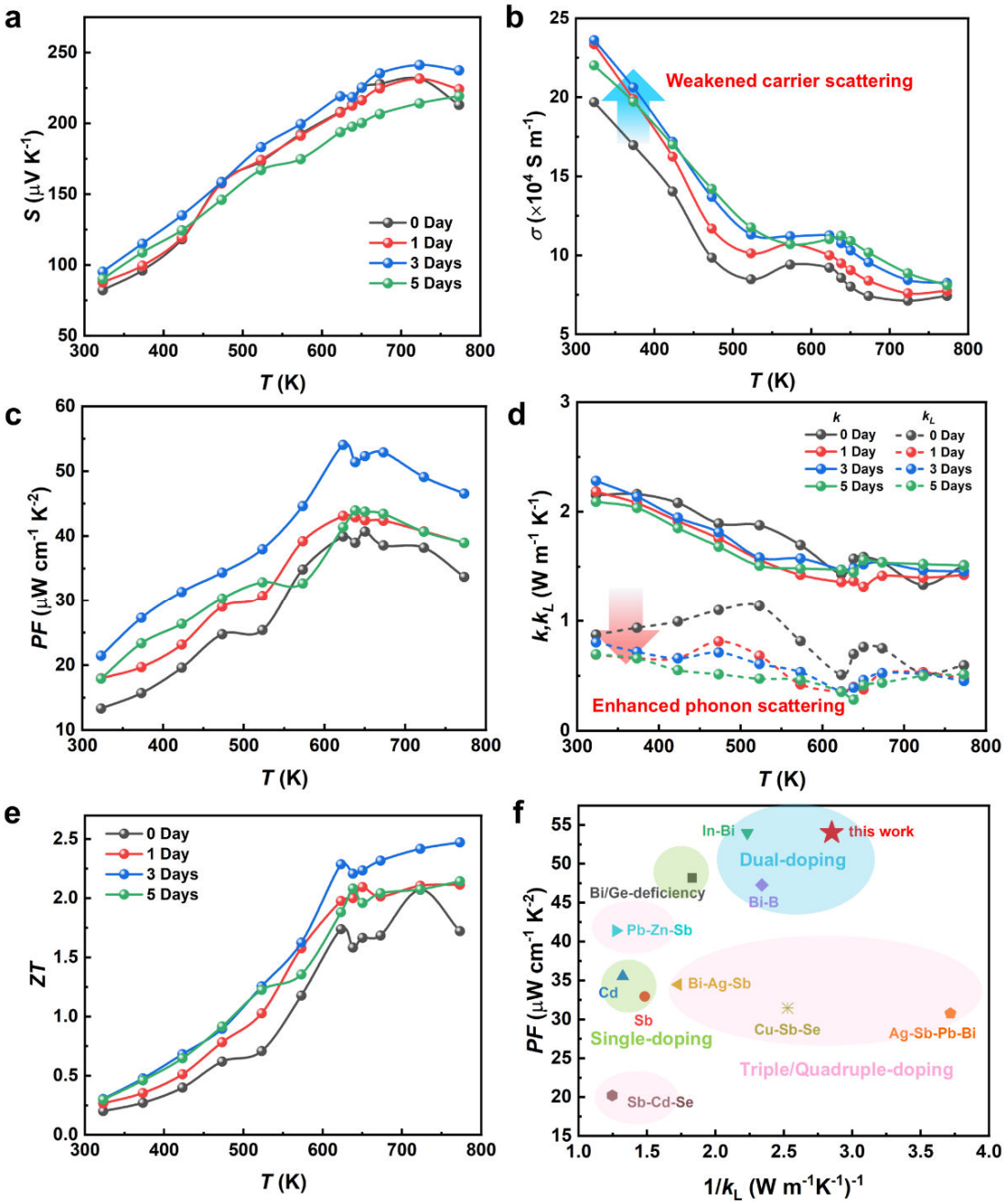

Figure S1. Thermoelectric properties of $Ge_{1.01}Sm_{0.03}Bi_{0.06}Te$ after different recrystallization annealing times. Temperature-dependent **(a)** Seebeck coefficient, **(b)** electrical conductivity, **(c)** power factor, **(d)** total and lattice thermal conductivity, **(e)** ZT, and **(f)** comparison of power factors (PF) and inversed lattice thermal conductivities ($1/k_L$) in this work with previous outstanding GeTe-based thermoelectric materials with different amounts of doping elements [1-10].

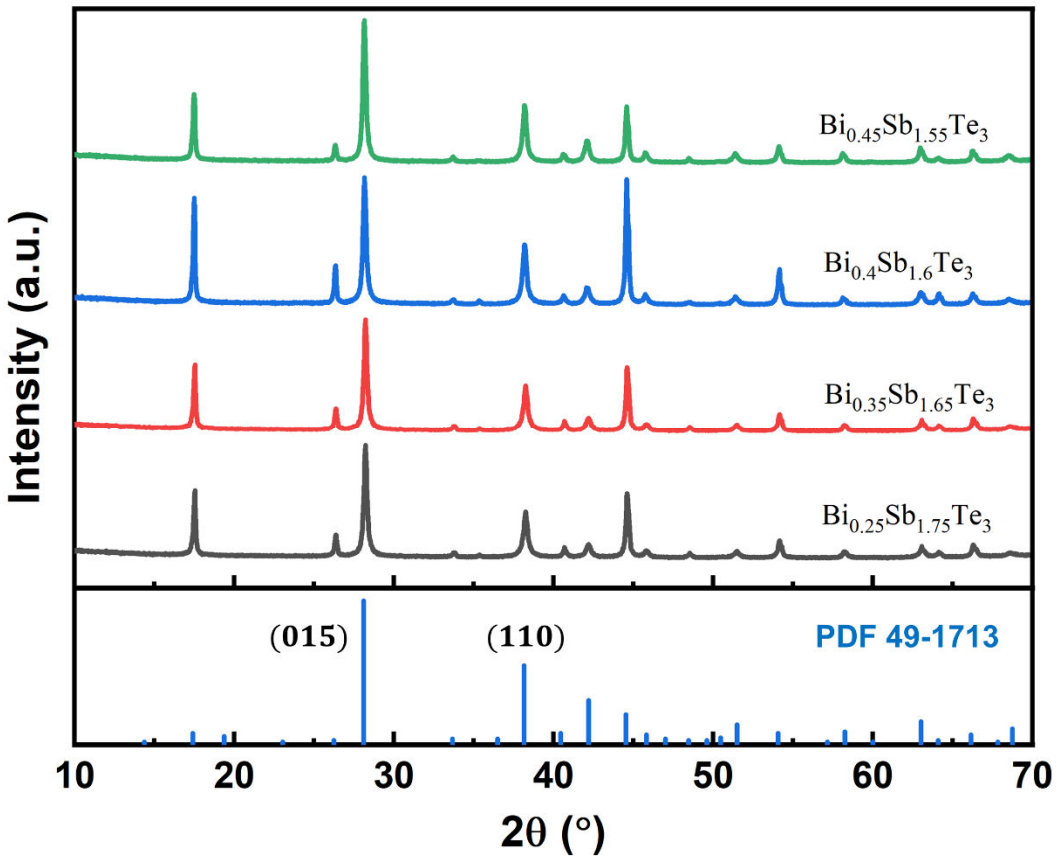

Figure S2. X-ray diffraction patterns of the p-type $Bi_{2-x}Sb_xTe_3$ samples.

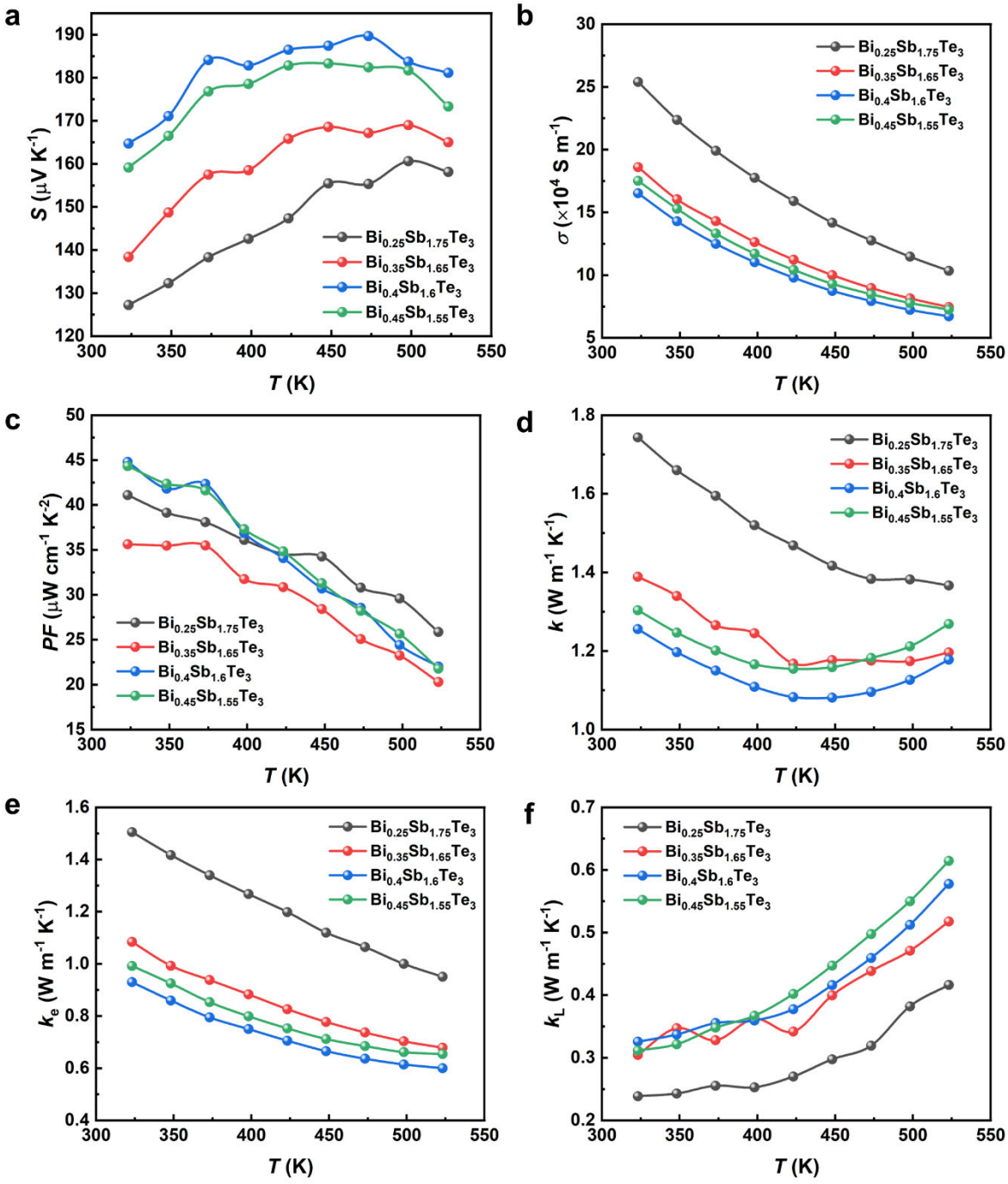

Figure S3. Temperature-dependent thermoelectric properties of p-type $Bi_{2-x}Sb_xTe_3$ samples. (a) Seebeck coefficient, (b) electrical conductivity, (c) power factor, (d)total thermal conductivity, (e) electrical thermal conductivity, and (f) lattice thermal conductivity.

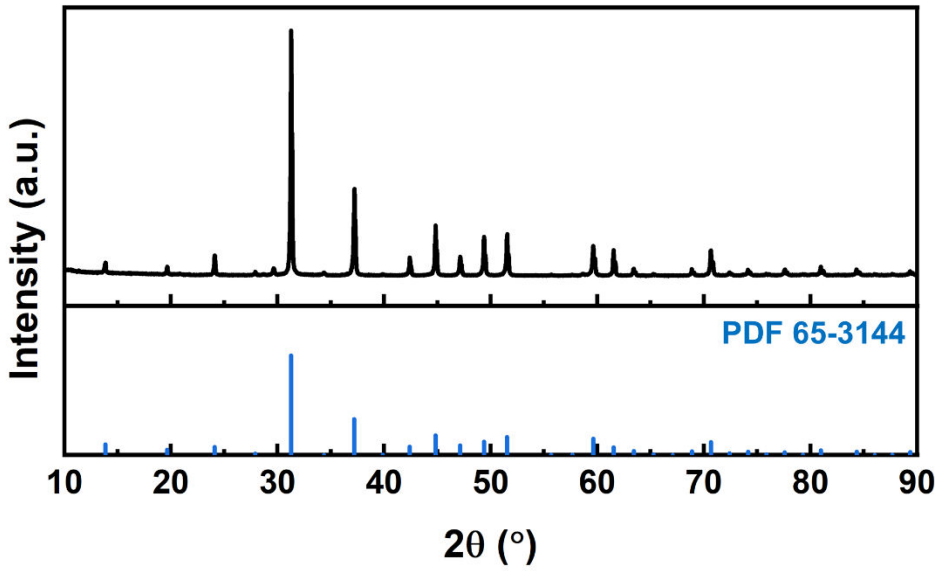

Figure S4. X-ray diffraction patterns of the n-type $Yb_{0.3}Co_4Sb_{12}$ sample.

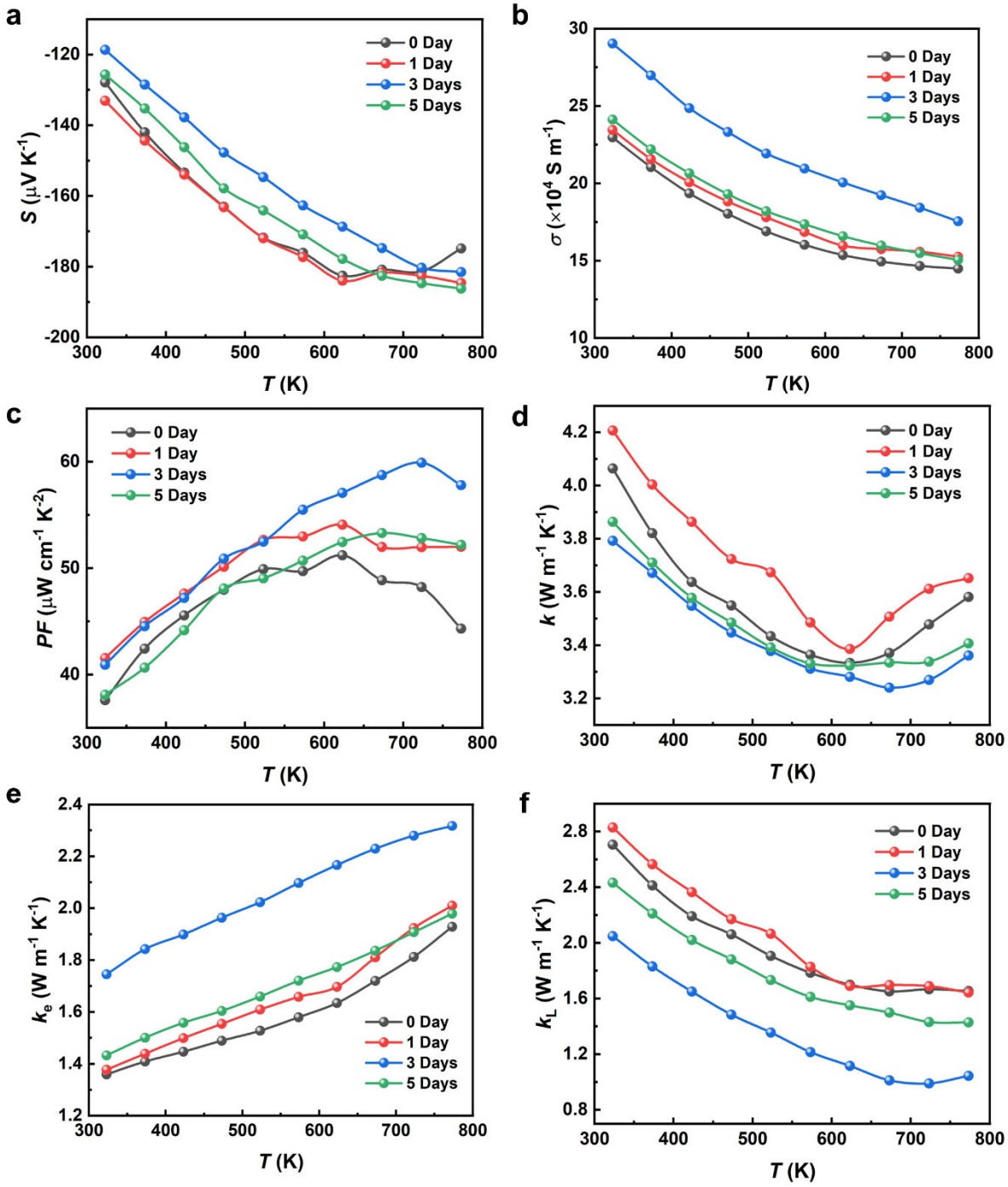

Figure S5. Temperature-dependent thermoelectric properties of n-type $Yb_{0.3}Co_4Sb_{12}$ samples with different annealing times (0~5 days). (a) Seebeck coefficient, (b) electrical conductivity, (c) power factor, (d)total thermal conductivity, (e) electrical thermal conductivity, and (f) lattice thermal conductivity.

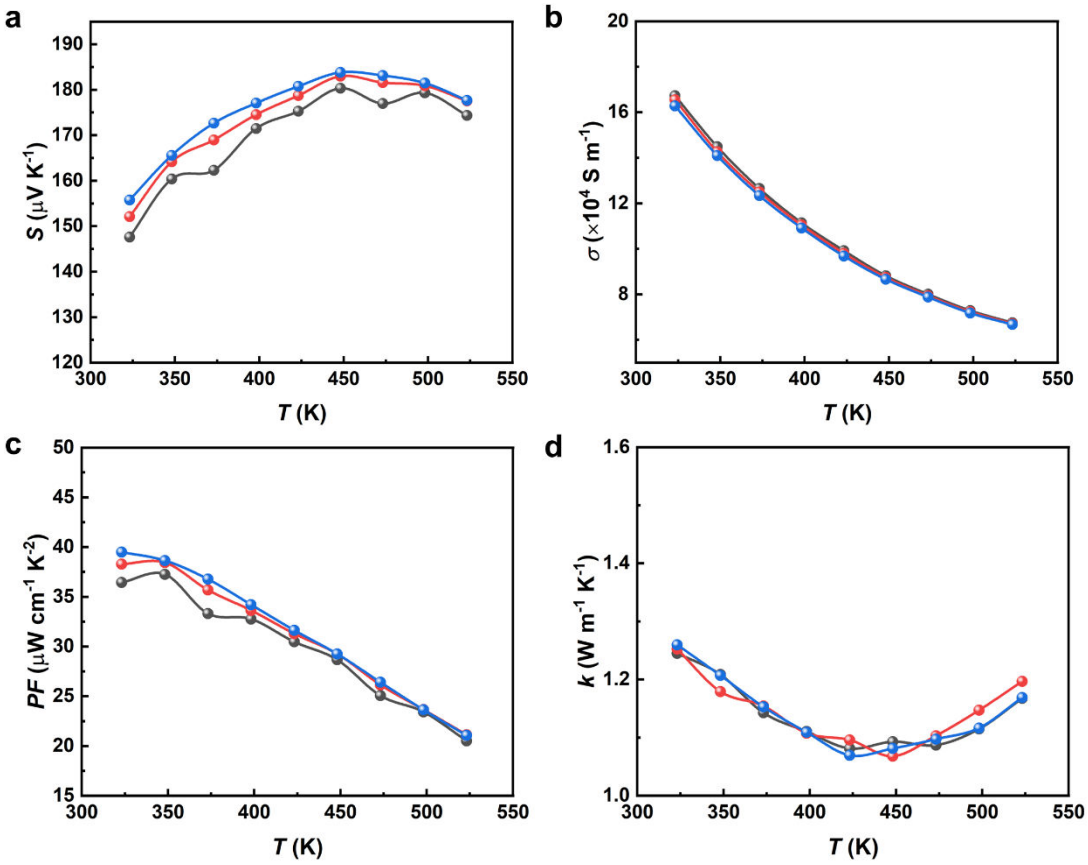

Figure S6. Repeated measurement of (a) Seebeck coefficient, (b) electrical conductivity, (c) power factor, and (d) total thermal conductivity of $Bi_{0.4}Sb_{1.6}Te_3$.

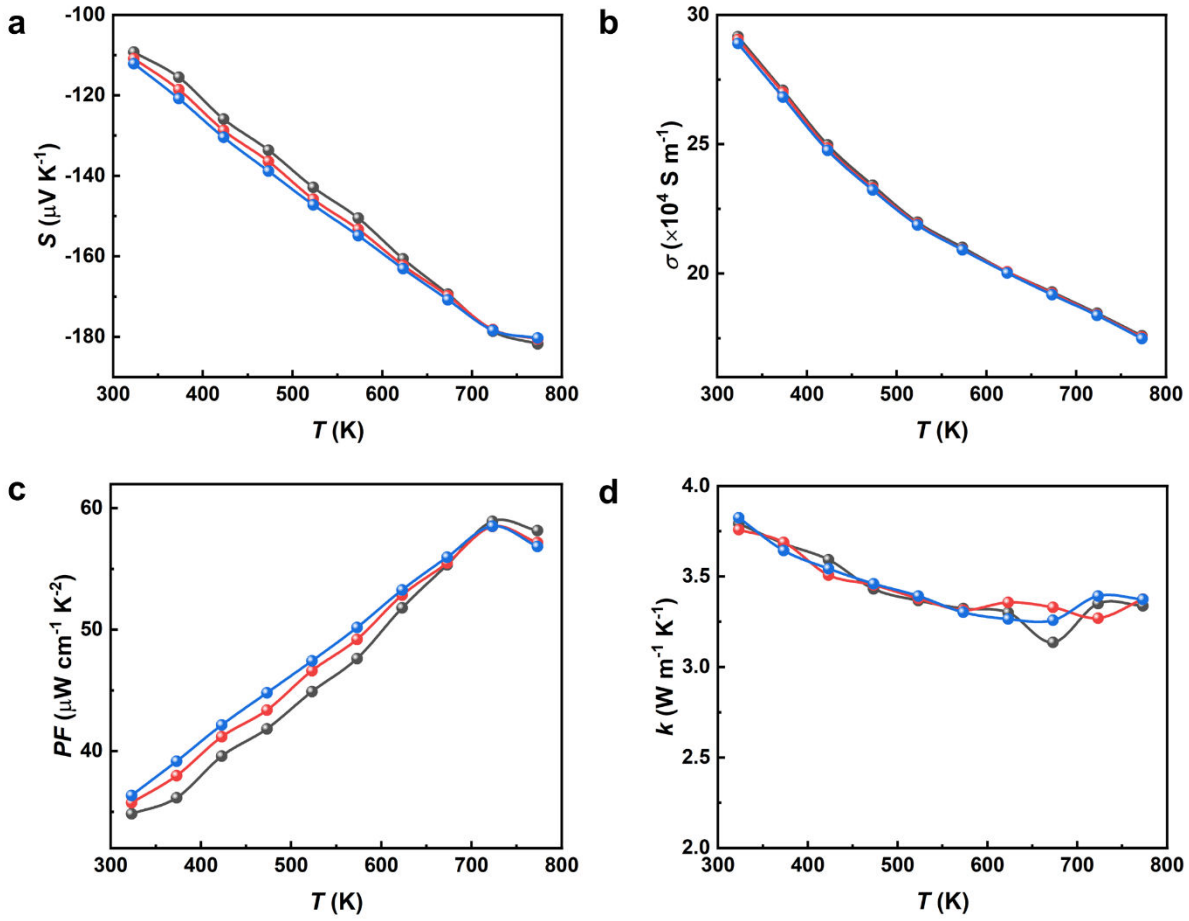

Figure S7. Repeated measurement of (a) Seebeck coefficient, (b) electrical conductivity, (c) power factor, and (d) total thermal conductivity of $Yb_{0.3}Co_4Sb_{12}$.

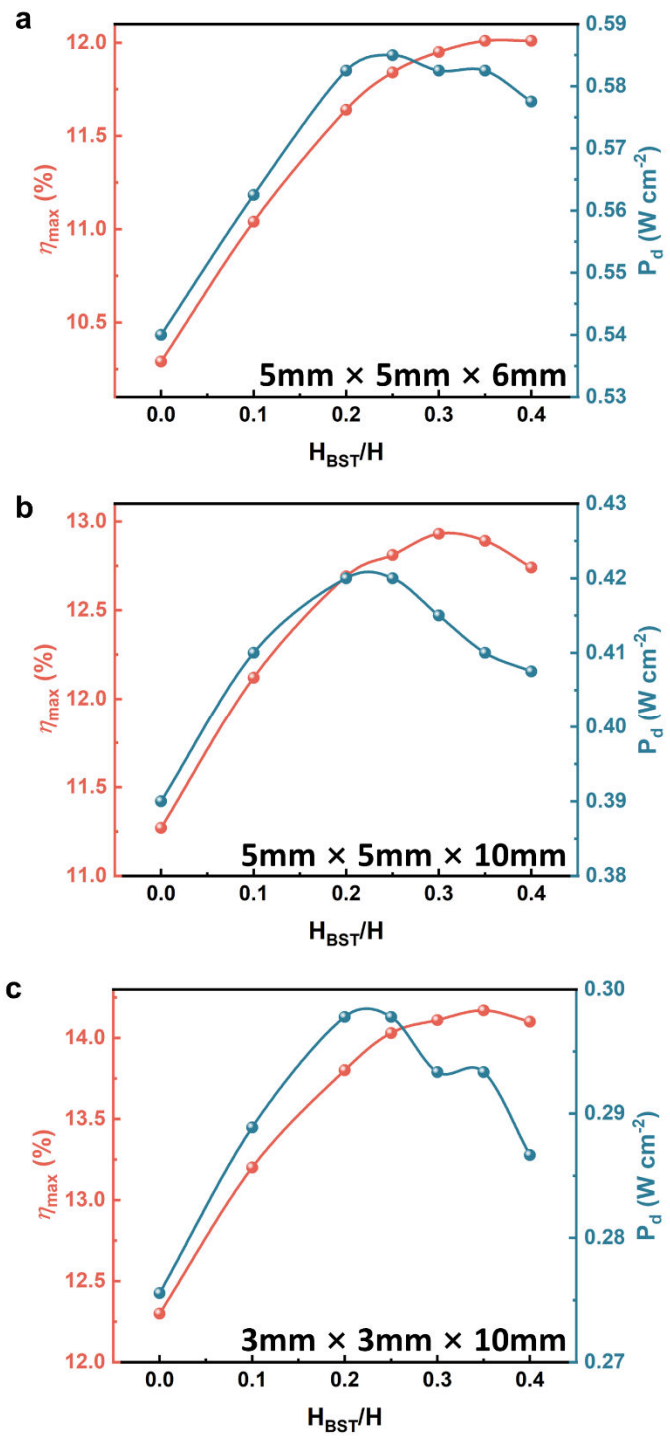

Figure S8. The Multiphysics-field FEM-predicted maximum energy conversion efficiency and power density with different segmentation ratios H_{BST}/H under a temperature difference of 500 K for: (a) $H/A_{pn} = 0.24$ mm^{-1}; $A_p/A_n = 1$, (b) $H/A_{pn} = 0.4$ mm^{-1}; $A_p/A_n = 1$, and (c) $H/A_{pn} = 1.1$ mm^{-1}; $A_p/A_n = 1$. The inset numbers denote the sizes of p and n-type thermoelectric legs.

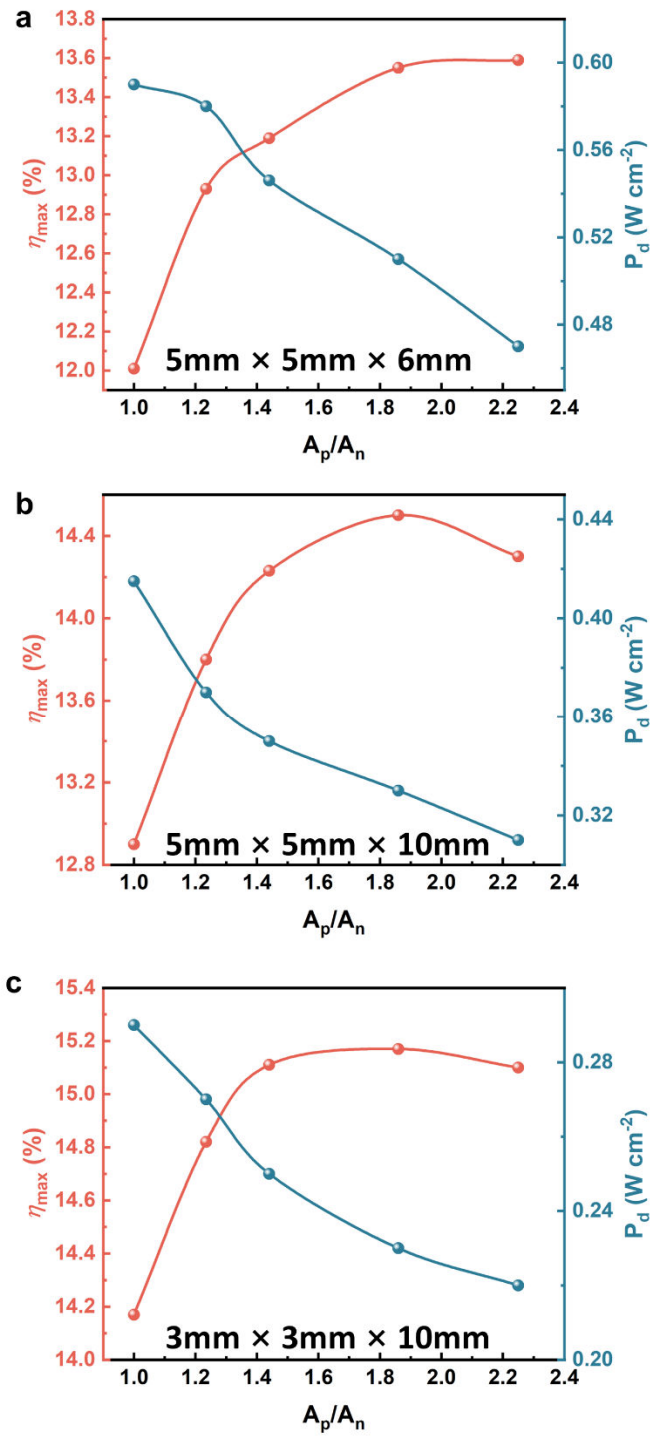

Figure S9. The Multiphysics-field FEM-predicted maximum energy conversion efficiency and power density with different cross-section area ratios A_p/A_n under a temperature difference of 500 K for: (a) H/A_{pn} = 0.24 mm^{-1}; H_{BST}/H = 0.35, (b) H/A_{pn} = 0.4 mm^{-1}; H_{BST}/H = 0.35, and (c) H/A_{pn} = 1.1 mm^{-1}; H_{BST}/H = 0.35. The inset numbers denote the sizes of p-type thermoelectric legs.

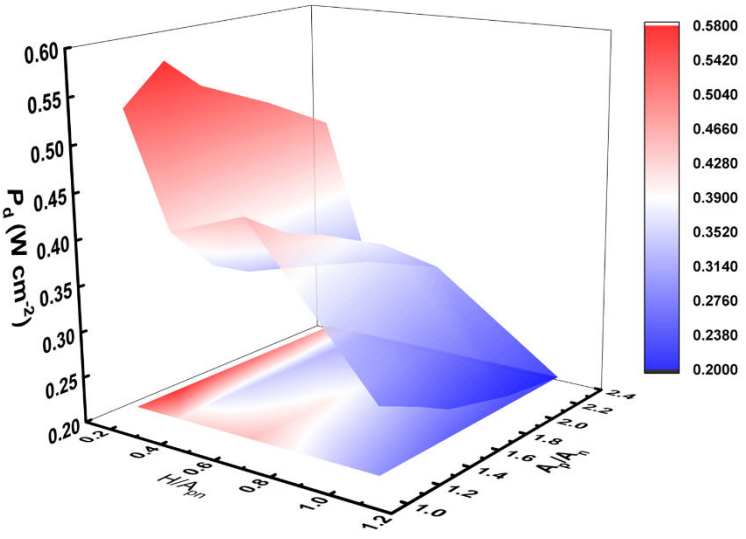

Figure S10. 3D diagram of the maximum power density surface P_d, predicted using Multiphysics-field FEM simulations.

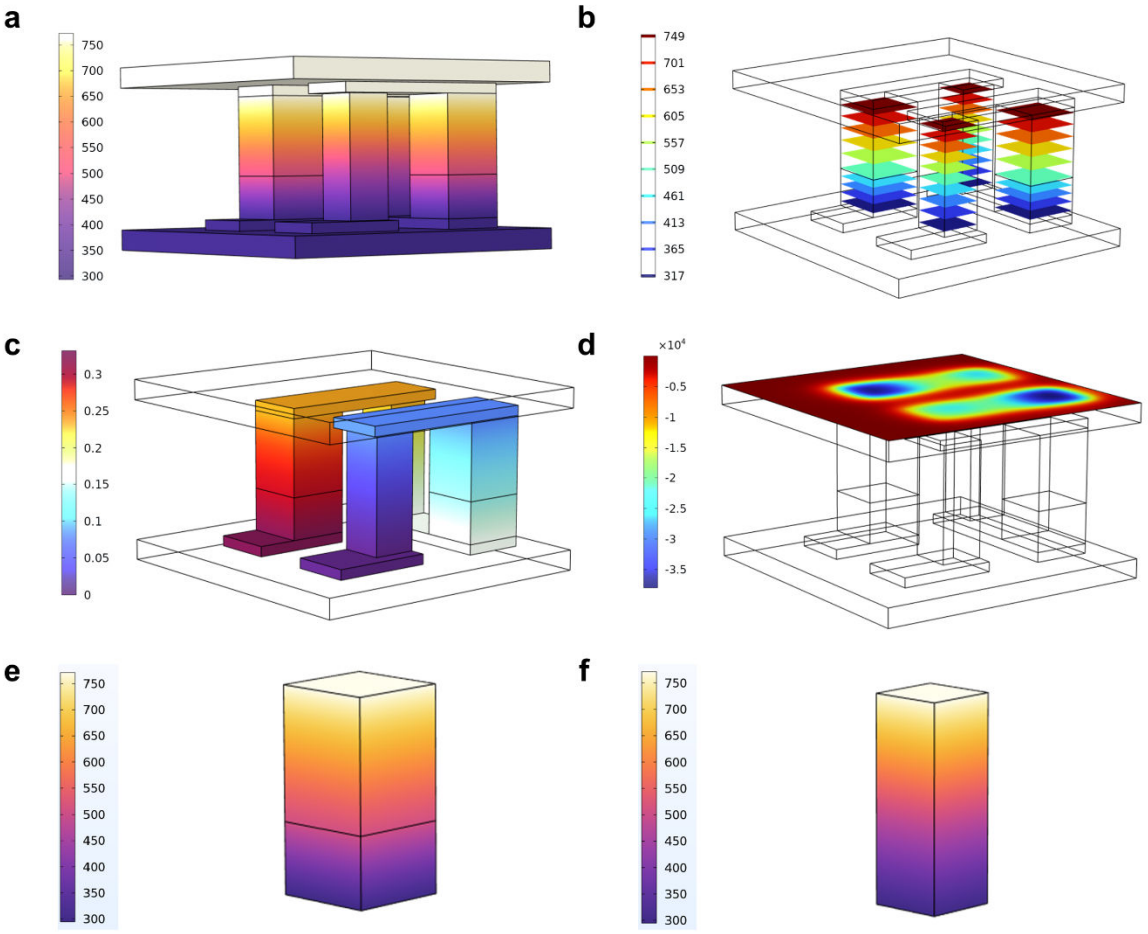

Figure S11. Multiphysics-field FEM simulated contours for optimized segmented thermoelectric module: (a) temperature distribution, (b) temperature isosurface, (c) output voltage, (d) heat flow at the hot side, and temperature distribution along the height for (e) the segmented p-type BST-GeTe leg and (f) the n-type SKD leg.

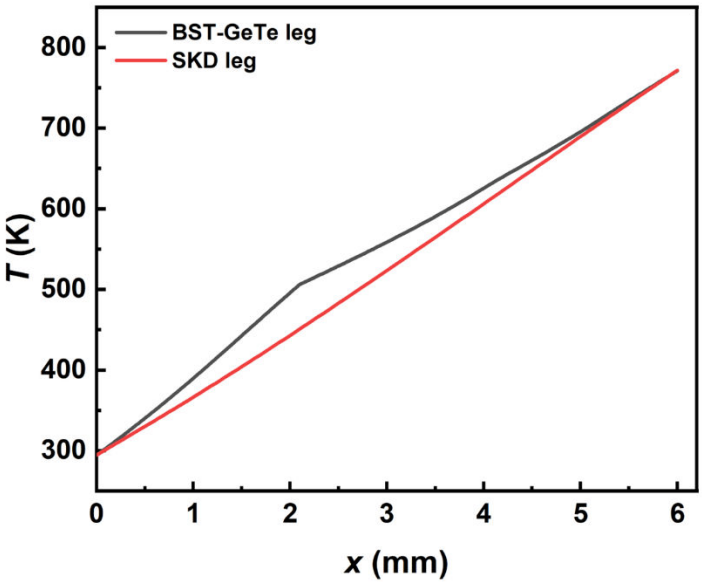

Figure S12. Multiphysics-field FEM simulated temperature distribution along the pillar height for the p-type BST-GeTe segmented leg and the n-type SKD leg.

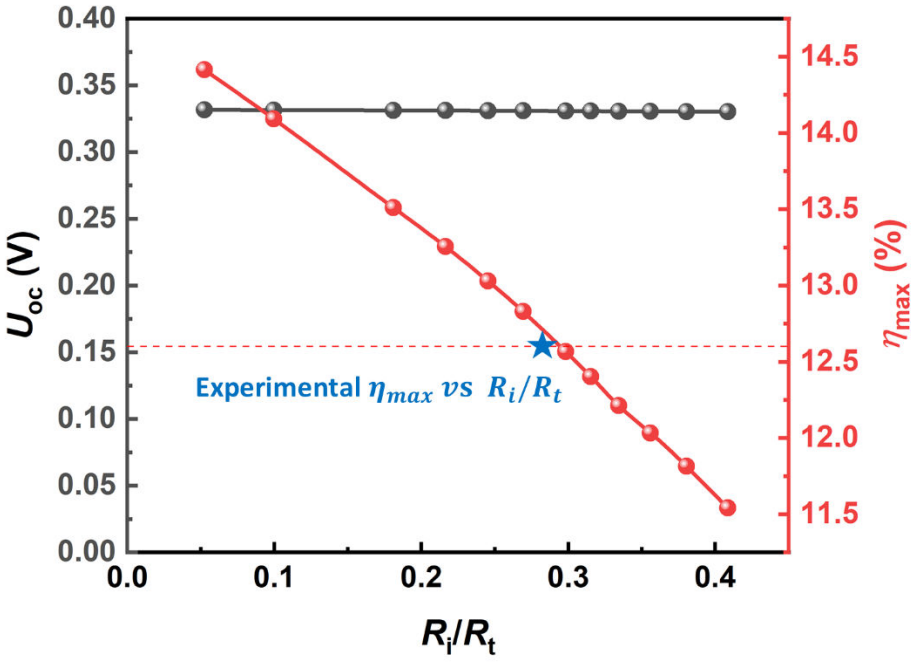

Figure S13. Plot of the open-circuit voltage U_{oc}, maximum energy conversion efficiency η_{max} with a function of R_i/R_t (the ratio between the internal contact electrical resistance R_i and the total internal resistance R_t), where the blue star represents the experimental results of η_{max} at $R_i/R_t \approx 0.28$. The experimental R_i was estimated by taking the difference between the measured total internal resistance R_t and the individual thermoelectric material and electrode resistances, and the results are in reasonable agreement with the simulations.

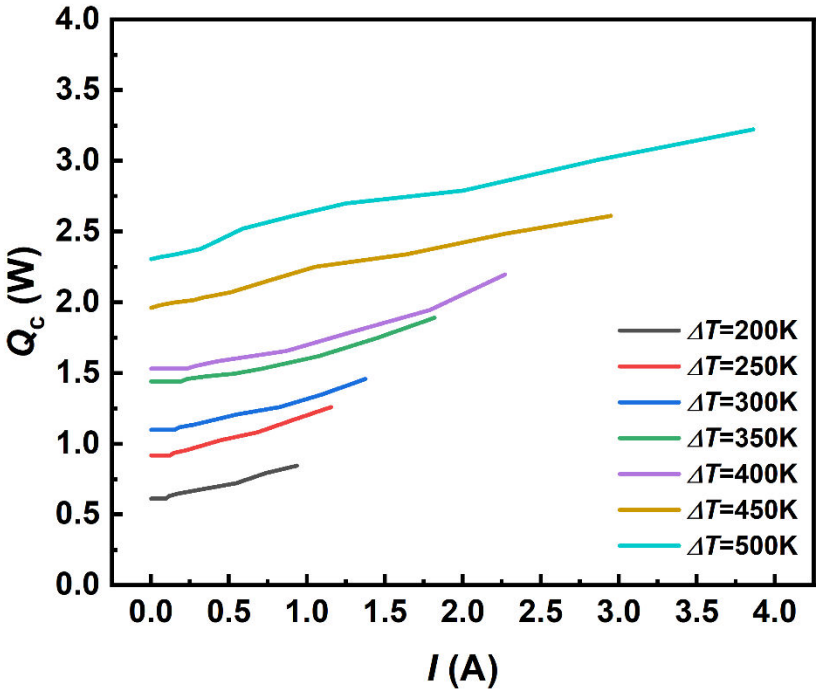

Figure S14. Experimentally measured current-dependent cold-side heat flow rate at different ΔT for the segmented TE module.

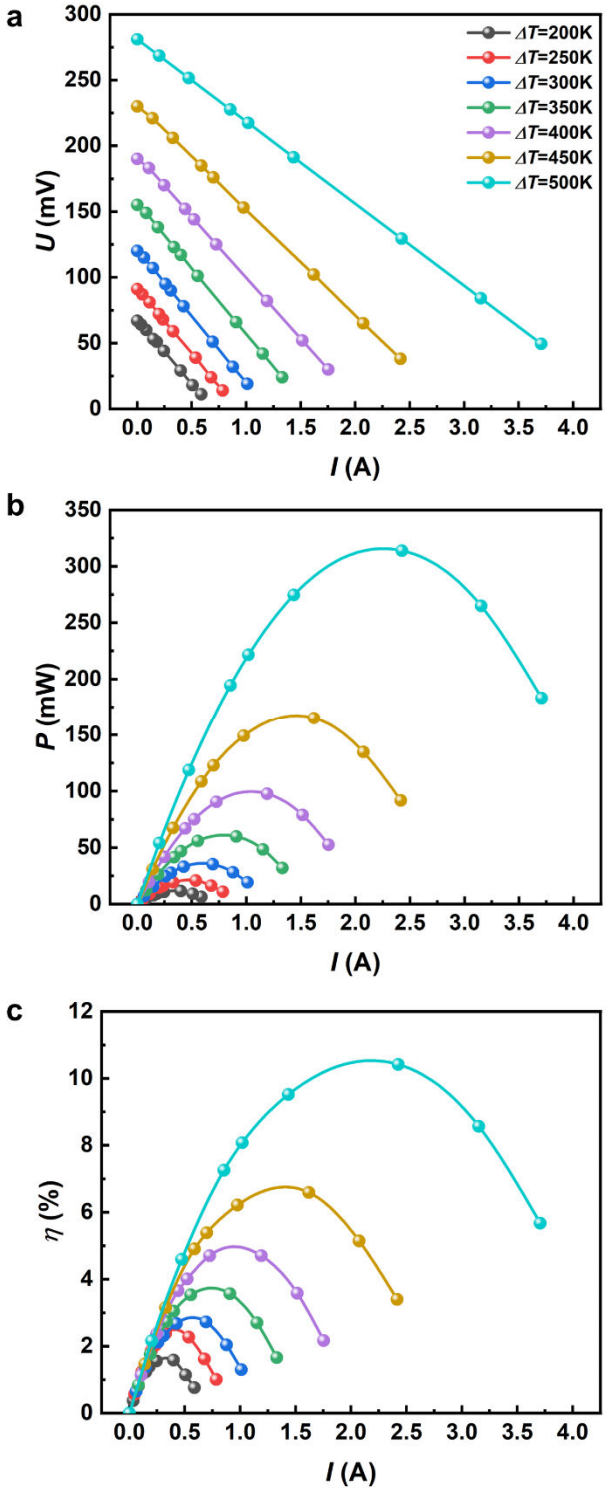

Figure S15. Experimentally measured current-dependent (a) output voltage, (b) output power, and (c) energy conversion efficiency at different ΔT for unsegmented TE module.

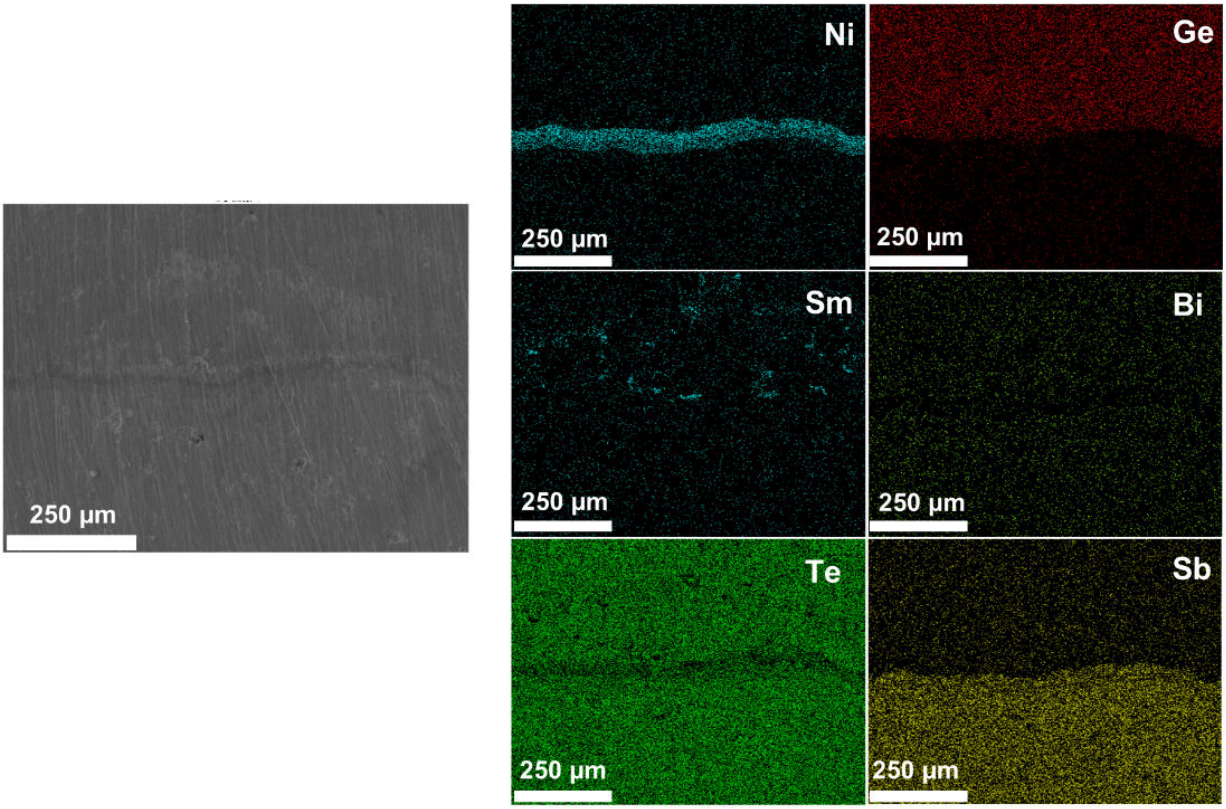

Figure S16. Energy dispersive X-ray spectroscopy (EDS) mapping of the interface in the (Bi, $Sb)_2Te_3$-(Ge, Sm, Bi)Te segmented leg after 2-cycle device testing.

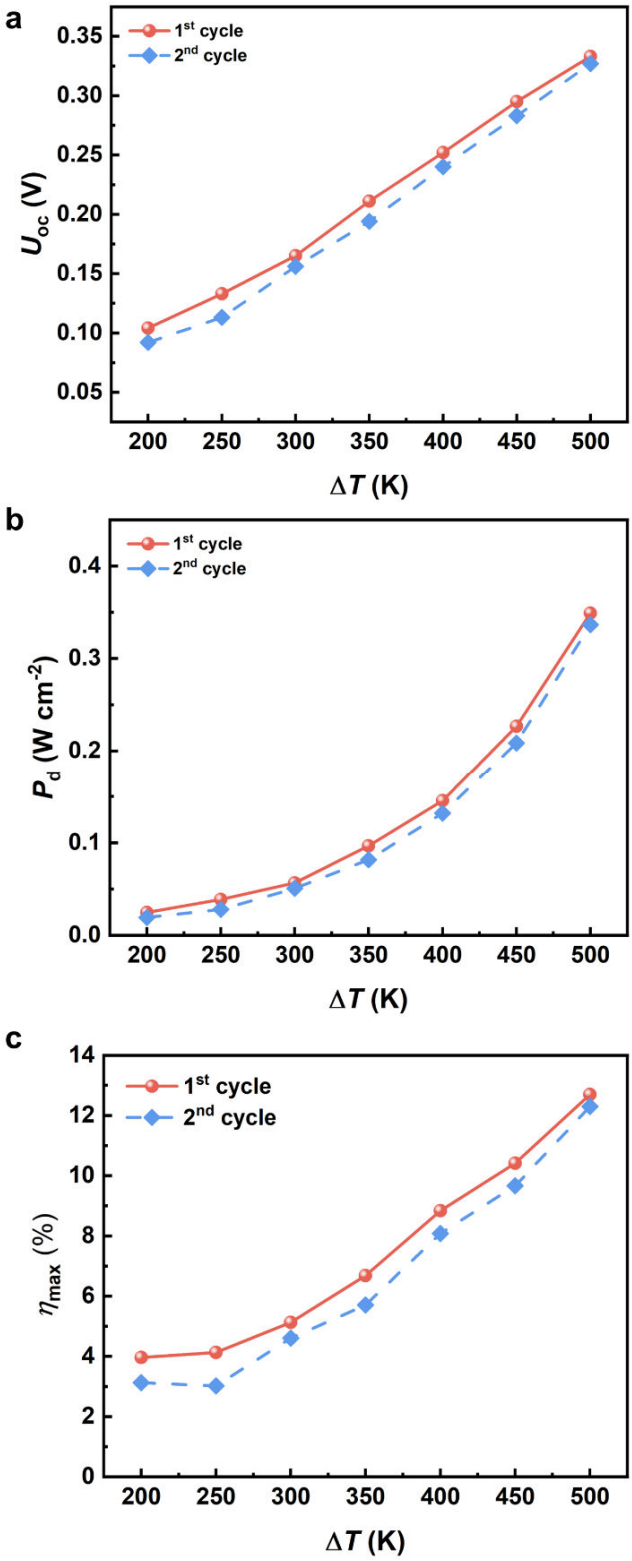

Figure S17. Comparison of (a) open-circuit voltage, (b) power density, and (c) maximum energy conversion efficiency of 2-cycle segmented module test.

Supplementary Note

The device-level energy conversion efficiency was evaluated using a thermoelectric testing system. The external and internal images of the thermoelectric device testing system are displayed in **Figure S18**. More details on the system can be found in our earlier work [11]. To eliminate the influence of natural convection on the measurement accuracy, the testing was conducted within a vacuum chamber maintained at a pressure around 5 Pa. All data acquisition and process controls were integrated into a centralized workstation, comprising a feedback-controlled power supply, an electrical measurement unit, and a high-precision data logger.

Thermal energy was supplied to the hot side of the device via a power-controllable silicon carbide (SiC) heater. A K-type thermocouple, attached to the edge of the device's hot junction, monitored the temperature in real-time, providing feedback to the power supply to maintain a stable hot-end temperature. Conversely, the cold side was coupled to an alumina oxide block of matching cross-sectional area, which was cooled by a water-circulation system with an adjustable flow rate. Two K-type thermocouples at the cold junction provided the necessary feedback to regulate the water flow, ensuring a constant cold-end temperature.

The Al_2O_3 block served as a heat flow meter. By measuring the temperature gradient between two internal points at a known distance using inserted K-type thermocouples, the heat flow passing through the device was calculated based on one-dimensional Fourier heat conduction law, utilizing the block's known thermal conductivity and cross-sectional area. The total input thermal power was determined by summing the transmitted heat and the internally generated Joule heat. The energy conversion efficiency was then defined as the ratio of the generated electrical output power to the total input thermal power. To minimize thermal contact resistance, a stepper motor-driven press was employed to maintain high contact pressure between the device and the heat/cold sources. Furthermore, high-conductivity graphite sheets were inserted at all interfaces to ensure optimal thermal coupling.

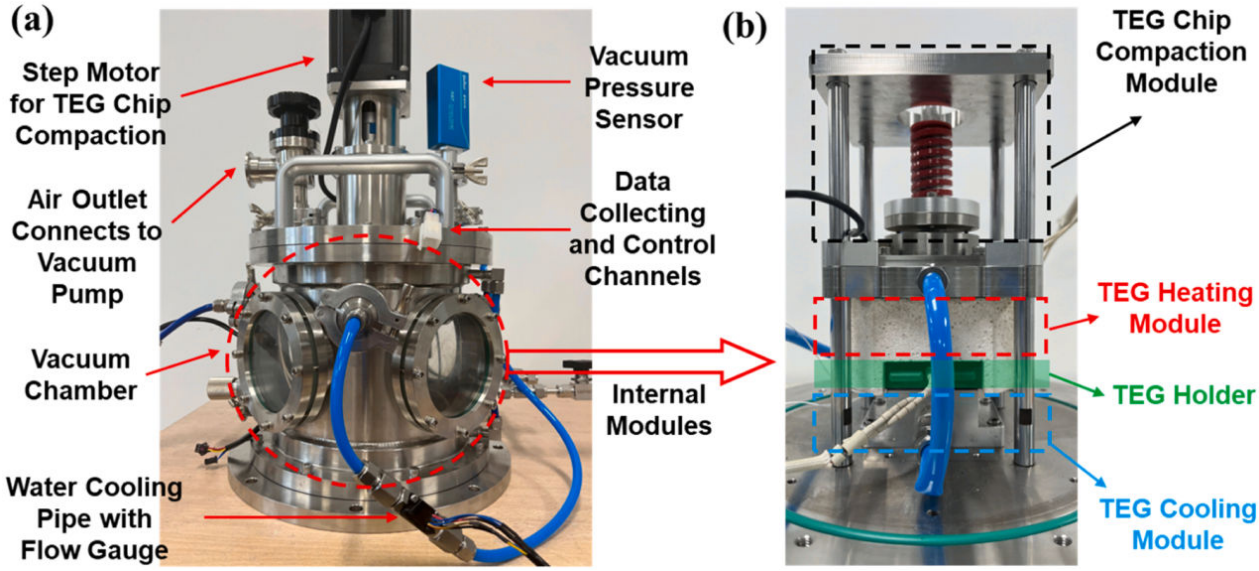

Figure S18. Pictures and layout of **(a)** the external structure of the thermoelectric device evaluation system, and **(b)** internal structure of the vacuum chamber [11].

Supplementary References

[1] Jiang Y, Su B, Yu J, et al., Exceptional figure of merit achieved in boron-dispersed GeTe-based thermoelectric composites, Nature Communications, 2024, 15: 5915.

[2] Jiang Y, Dong J, Zhuang H L, et al., Evolution of defect structures leading to high ZT in GeTe-based thermoelectric materials, Nature Communications, 2022, 13: 6087.

[3] Chen S, Bai H, Li J, et al., Vacancy-Based Defect Regulation for High Thermoelectric Performance in $Ge_9Sb_2Te_{12-x}$ Compounds, ACS Appl Mater Interfaces, 2020, 12: 19664-19673.

[4] Hong M, Wang Y, Liu W, et al., Arrays of Planar Vacancies in Superior Thermoelectric $Ge_{1-x-y}Cd_xBi_yTe$ with Band Convergence, Advanced Energy Materials, 2018, 8: 1801837.

[5] Perumal S, Samanta M, Ghosh T, et al., Realization of High Thermoelectric Figure of Merit in GeTe by Complementary Co-doping of Bi and In, Joule, 2019, 3: 2565-2580.

[6] Li H, Chen C, Cheng J, et al., Lead-free GeTe alloys with high thermoelectric performance for low-grade waste heat energy harvesting, Nano Energy, 2025, 136: 110690.

[7] Liu S, Wang W, Xie L, et al., Realizing High Thermoelectric Performance in GeTe-Based Alloys Without Lead Addition, Advanced Functional Materials, 2025: e10362.

[8] Wang Z, Wu H, Zhang B, et al., Phase Modulation Enabled High Thermoelectric Performance in Polycrystalline $GeSe_{0.75}Te_{0.25}$, Advanced Functional Materials, 2022, 32: 2111238.

[9] Jin Y, Qiu Y, Bai S, et al., Modifying Roles of $CuSbSe_2$ in Realizing High Thermoelectric Performance of GeTe, Advanced Energy Materials, 2024: 2400623.

[10] Jiang B, Wang W, Liu S, et al., High figure-of-merit and power generation in high-entropy GeTe-based thermoelectrics, Science, 2022, 377: 208-213.

[11] Duan Y, Lin S, Bai Y, et al., Experiment-Validated multiphysics modeling, generalizable deep learning and interpretable global sensitivity analyses for thermoelectric generators, International Journal of Heat and Mass Transfer, 2024, 229: 125711.